PHYSICAL REVIEW B **81**, 014425 (2010)

Spin-wave transduction at the submicrometer scale: Experiment and modeling

V. Vlaminck and M. Bailleul*

Institut de Physique et Chimie des Matériaux de Strasbourg, UMR 7504 CNRS, Université de Strasbourg, 23 rue du Loess, BP 43, 67034 Strasbourg Cedex 2, France

(Received 14 September 2009; revised manuscript received 4 January 2010; published 29 January 2010)

We report a complete study of spin-wave transduction combining microwave measurements performed over a frequency range of [1–15] GHz on Permalloy strips (thickness=10–20 nm, width=2–8 μm) and an accurate modeling of the experiment. This technique has been used recently to assess the spin polarization of the electrical current by measuring a current-induced spin-wave Doppler shift. We present here an electromagnetism calculation based on the magnetostatic wave theory combined with the Gilbert form of the damping that can be used directly as an optimization tool for future spin-wave experiments.

DOI: 10.1103/PhysRevB.81.014425 PACS number(s): 76.50.+g, 41.20.−q, 72.25.Ba

I. INTRODUCTION

When the magnetization of a ferromagnet is tilted away from its equilibrium direction at one point, this perturbation propagates in the form of a so-called spin wave. The study of spin waves in thin metal films, commonly encountered in modern magnetic recording and spintronics devices, is emerging as a distinct subfield of magnetism. Indeed, spin waves were proposed as a mean of routing and processing electrical signals.[1,2] From a fundamental point of view, spin waves are able to interact with micromagnetic structures such as domain walls and vortices.[3–6] Recently, we have shown that sub-micrometer wavelength spin waves could be used to probe spin-polarized transport in a ferromagnetic metal.[7] In these developments, it is essential to be able to launch spin waves with short-enough wavelength in a controlled manner.

A propagating spin wave is conveniently generated using the spatially inhomogeneous microwave magnetic field generated by a set of conductors (spin-wave antenna). The spin waves can be detected either inductively by a second antenna (a technique called PSWS, namely, propagating spin-wave spectroscopy) (Refs. 8–11) or by optical means.[12–14] Time-domain techniques using short magnetic field pulses can also be used both with electrical and optical detections.[15–17] For the future developments of spin-wave techniques, it is highly desirable to dispose of a quantitative tool for describing the efficiency of the excitation process (spin-wave transduction) but also for interpreting the measured spectra and/or for predicting them. Several calculation methods have been developed in the past.[18–25] In the 1970s and 1980s, PSWS was used extensively in insulating yttrium iron garnet (YIG) films[18,26,27] which, due to their ultralow microwave losses, enable propagation of spin waves over several millimeters. In the calculations, the losses in the ferromagnetic material were ignored and the only parameter which was calculated is the radiation resistance of the excitation antenna. Due to these limitations, such calculations cannot be used to interpret PSWS measurements in thin metal films, where the losses (intrinsic damping) play an essential role. In this paper, we describe a calculation method well-suited for interpreting propagating spin-wave measurements in thin ferromagnetic metal films. We present measurements of spin-wave propagation conducted on an aggressive submicrometer length scale and we discuss the agreement between theory and experiment.

The paper is organized as follows. The device and the experimental principle used in our miniaturized version of PSWS are described in Sec. II. In Sec. III, we present typical microwave measurements and give a qualitative understanding of the obtained spectra. The electromagnetic model is treated in Sec. IV, in which we describe each step of the calculation. In Sec. V, we compare the measured spectra to the simulated ones and discuss the limitations of our approach. We separately treat the Fourier transform of the current distribution for a given antenna in the Appendix.

II. EXPERIMENT

A. Elaboration of a device

A typical microfabricated sample used for the PSWS experiment is shown in Fig. 1(a). The horizontal track in the middle is a $w=2$ μm Permalloy ($Ni_{80}Fe_{20}$) strip. Close to the center of this strip, one distinguishes two meander-shaped patterns which will serve as spin-wave antennae. These antennae are zoomed in Fig. 1(b). Each of them can be viewed as a coplanar waveguide (i.e., one signal track with two lateral ground tracks) shrunken to a sub-micrometer size and folded five times onto itself. As explained below, this meander shape allows one to precisely define the wavelength of the spin wave and to optimize the transduction efficiency. At one extremity of the antenna, the signal and the ground tracks are short-circuited [center of Fig. 1(b)]. At the other extremity, the antenna is connected to a wider coplanar waveguide [the three tracks on the left and on the right of Fig. 1(a)] for injecting and measuring the microwave signal. The devices were fabricated in the aim of the current-induced Doppler shift experiment,[7] so that they contain the electrical contacts for the injection of a dc current through the strip [see the four vertical tracks in Fig. 1(a)] that would not be necessary for the present study.

The elaboration of a device begins with the sputtering of a Permalloy film ($t=10–20$ nm) with a 15 nm capping of alumina on a ~ 1 cm^2 intrinsic silicon substrate that has a 300-nm-thick thermal oxide layer. In the first stage, the Permalloy

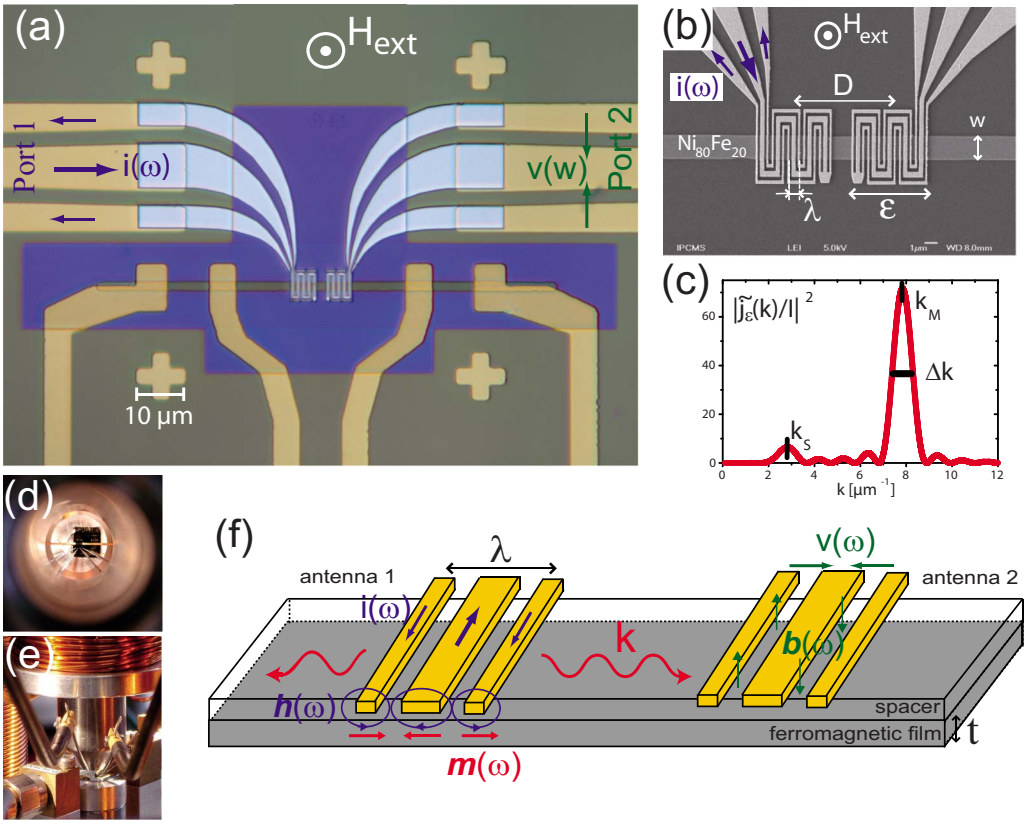

FIG. 1. (Color online) (a) Optical microscope picture of a propagating spin-wave spectroscopy device (w=2 μm, λ=800 nm, five meanders, D=7.8 μm). (b) Scanning electron microscope picture of the center part of the same device. (c) Fourier transform of the spatial profile of the linear density of the microwave current corresponding to this device. [(d) and (e)] Pictures of the sample laying on the lower pole of the electromagnet and in contact with the two microwave probes (and four tungsten dc tips). (e) Upper pole piece of the electromagnet being removed as seen from above. (e) Upper pole piece being inserted as seen from the side. (f) Sketch of the operating principle of propagating spin-wave spectroscopy.

strips are patterned by optical lithography (image reversal process) followed by a lift-off of aluminum [t(Al)=50 nm] and Ar^+ ion-beam etching. The dry etching is performed at an angle of 40° to limit the redeposition and the sample is disposed on a rotative chuck to improve the homogeneity of the etching. In the second stage, optical lithography followed by a lift-off of Cr(5 nm)-Au(100 nm) is used to make the dc electrical contacts, the connecting part of the coplanar waveguides, and the alignment cross marks. The third stage consists in depositing a sufficiently thick insulating pattern above the Permalloy strip to avoid electrical short circuits between the waveguide and the strip. For this purpose, a 90-nm-thick pattern of cross-linked PMMA (polymethylmethacrylate) was obtained by exposing the resist to a very high electron dose (~14000 μC cm^{-2}). Finally, in the last stage, the spin-wave antennae are patterned by electron-beam lithography, exposing a 350 nm PMMA layer to a 30 kV-40 pA beam with a dose of about 400 μC cm^{-2}. This is followed by an oxygen plasma clean (to guarantee the electrical contacts with the coplanar waveguides fabricated in the second stage) and the lift-off of a Cr(5 nm)/Al(150 nm) layer. In addition to the sample shown in Figs. 1(a) and 1(b), we fabricated and measured seven other devices for which we varied the size of the meander that sets the wavelength of the spin wave (λ=0.8 and 1.6 μm), but also the number of meanders (3 and 5), the distance D between the two antennae (D=5–8–15 μm), the thickness (t=10 and 20 nm), and the width (w=2, 3.5 and 8 μm) of the Permalloy strip.

B. Measurement setup

The fabricated device is placed in the center of the lower pole of an electromagnet fitting in a home-made probe station.[28] The upper pole of the electromagnet is first removed for optical access, allowing one to contact the microwave probes (GGB industries) to the coplanar waveguides [Fig. 1(d)]. The upper pole is then inserted [Fig. 1(e)] and a vertical field is generated in the 2 mm gap (+/−1.5 T with a +/−5 A current in the coils). The Joule heating of this electromagnet is the main limiting factor for the stability of the experiment.

The microwave probes are connected to a vector network analyzer (VNA, Agilent E8362B, 10 MHz-20 GHz) via phase-stable coaxial cables. The microwave apparatus is calibrated with the use of a calibration substrate that contains short-open-50 Ω load-through coplanar standards. An electrical delay is added to account for the propagation of the microwave signal from the probe to the antenna along the 0.9 mm coplanar waveguide. The impedance of the antenna ranges between 50 and 80 Ω in order to respect the 50 Ω impedance matching as much as possible.

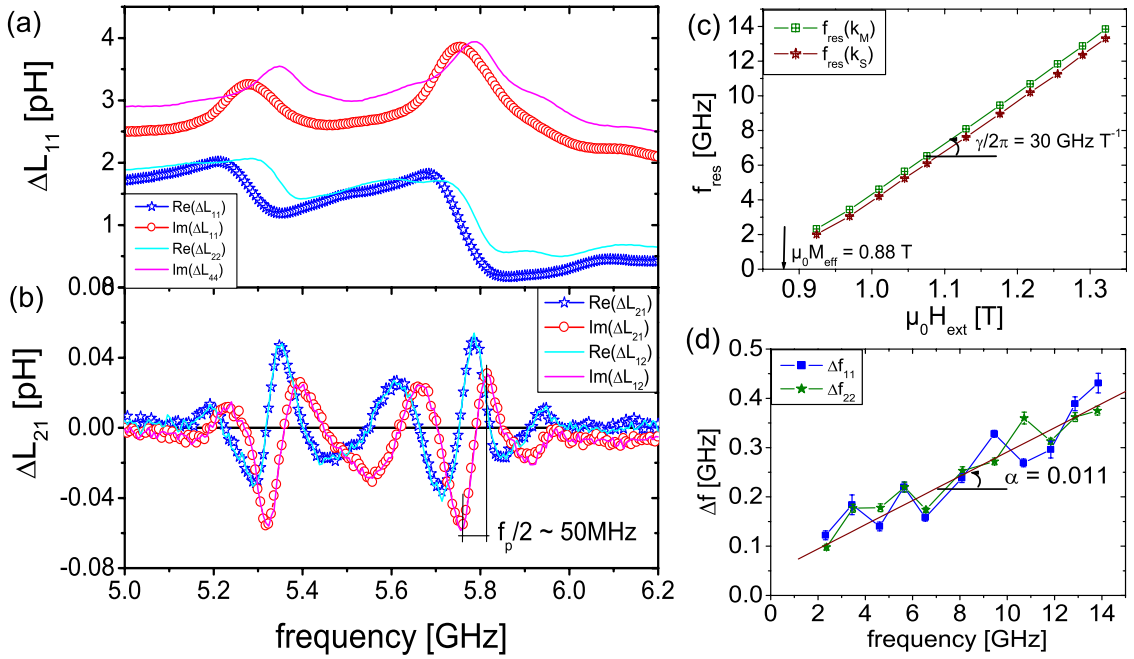

FIG. 2. (Color online) (a) Self-inductance ΔL_{11} and ΔL_{22} and (b) mutual inductance ΔL_{12} and ΔL_{21} measurements for the device shown in Fig. 1(a) ($\lambda=800$ nm, $D=7.8$ μm, $t=20$ nm, and $w=2$ μm) subjected to a field $\mu_0 H_{ext}=1.047$ T ($\mu_0 H_{ref}\simeq 1.117$ T). [(c) and (d)] FMR characterization of the strip from the self-inductance measurements. (c) Magnetic field dependence of the two main resonance frequencies. (d) Frequency dependence of the frequency swept line width (FWHM).

C. Operating principle

The operating principle, which is represented in Fig. 1(f), is the following. We first inject a microwave current $i(\omega)$ into antenna 1 via the vector network analyzer. This generates a high-frequency field $\mathbf{h}(\omega)$. Owing to the meander shape of the antenna, $\mathbf{h}(\omega)$ has a spatial periodicity λ ($\lambda\sim 800$ nm for the device shown in Fig. 1). Then, this microwave field excites spin-wave modes of wavelength peaked around λ, which propagate in both directions along the ferromagnetic strip. Finally, the spin wave generates an additional magnetic flux on the antennae, which, according to Faraday's law, induces a voltage $v(\omega)$. This voltage is measured with the help of the network analyzer both on the excitation antenna (port 1) and on the second reception antenna (port 2). In a subsequent measurement, the microwave current is injected into port 2, so that antenna 2 becomes the excitation antenna and antenna 1 becomes the detection antenna. More precisely, from the S parameters delivered by the network analyzer, we extract the impedance matrix Z_{nm} [$v_n=\Sigma_m Z_{nm} i_m$, where $(n,m)=(1,2)$ are the port or antenna number]. Note that the antennae are much shorter than an electrical wavelength so that a localized impedance model can be used.

As the coupling between the antennae and the ferromagnetic strip is purely inductive, we work with the inductance matrix as a response function. We always perform two measurements: the first one $Z_{nm}(\omega,H_{res})$ at a resonant field in accordance with the dispersion of the excited spin-wave mode and a second one at a reference field $Z_{nm}(\omega,H_{ref})$, for which no resonant behavior occurs within the frequency range we sweep. The subtraction of the two measurements leads to the spin-wave contribution of the inductance matrix: $\Delta L_{nm}(\omega)=\frac{1}{i\omega}[Z_{mn}(\omega,H_{res})-Z_{mn}(\omega,H_{ref})]$. From the self-inductances ΔL_{11} and ΔL_{22}, one can extract the efficiency of the excitation of the spin waves by the antennae. From the mutual-inductances ΔL_{12} and ΔL_{21}, one can extract the propagation characteristics of the spin wave between the two antennae, which constitutes the PSWS measurement.

The injected power in the antenna needs to be limited to $P=-35$ dBm in order to stay in a linear-response regime (large distortions of the resonances were observed at higher power, which we interpret as a signature of nonlinear magnetization dynamics). The noise floor of the VNA receivers lays around $N=-130$ dBm for a 10 Hz bandwidth, so that a detection threshold estimate is $S_{nm}^{lim}=\sqrt{N/P}=-95$ dB. According to the $S_{nm}\leftrightarrow Z_{nm}$ relationships[29] and assuming the input impedance of the antenna Z to be close to the characteristic impedance $Z_c=50$ Ω, the smallest variation of impedance we can detect is $\delta Z_{nm}^{lim}=\frac{dZ_{nm}}{dS_{nm}}S_{nm}^{lim}=\frac{Z_c}{2}\sqrt{N/P}(1+Z/Z_c)^2=1.5$ mΩ. And so, the minimum inductance we can resolve at $f=10$ GHz is $\delta L_{nm}^{lim}=\delta Z_{nm}^{lim}/2\pi f=50$ fH. This detection threshold is of the same order as the intensity of the transmitted spin-wave signal that we detect with the device of Fig. 1(a) [see the spectrum in Fig. 2(b)]. As a consequence, an averaging of more than 100 scans is needed to bring the mutual-inductance signal clearly out of the noise floor.

To conclude this section, let us discuss the wave-vector distribution of the excited spin waves, which is given by the Fourier transform $\tilde{j}_\epsilon(k,\omega)$ of the linear microwave current density $j_\epsilon(x,\omega)$ [see Eq. (18)]. The normalized quantity $|\tilde{j}_\epsilon(k)/I|^2$ corresponding to the antenna of Fig. 1(a) is shown in Fig. 1(c). It displays a main peak at $k_M=7.8$ μm^{-1}, which corresponds to the spatial periodicity of the meander $\lambda\sim 800$ nm, and that has a full width at half maximum

(FWHM) of about 0.9 μm^{-1}. A secondary peak, less intense, appears at lower wave vectors $k_S=2.8$ μm^{-1}. This secondary peak is due to the design of the antenna. The design choice is explained in the Appendix, where the whole calculation of the Fourier transform $\tilde{j}_\epsilon(k)$ is presented.

III. MEASURED SPECTRA

In this section, the spin-wave dispersion which sets the frequency of the PSWS signal is given first. Then typical measurements of both the self-inductance and mutual inductance are presented and discussed.

A. Spin-wave dispersion

In this paper, we will only present results obtained with the field applied perpendicular to the plane of the sample. In this configuration, we excite the so-called magnetostatic forward volume waves (MsFVW), whose dispersion relation for the case of a thin film is written as[30]

$$\omega(k)^2 = \omega_H\left[\omega_H + \omega_M\left(1 - \frac{1-\exp(-k_\parallel t)}{k_\parallel t}\right)\right], \qquad (1)$$

with $\omega_M=\gamma\mu_0 M_s$ and $\omega_H=\gamma\mu_0 H_{equ}$, where γ is the gyromagnetic ratio, μ_0 is the permeability of vacuum, M_s is the saturation magnetization, and H_{equ} is the equilibrium field that contains the applied field H_{ext}, the static dipolar field which writes $H_d=-M_s$ in the thin-film approximation, and if necessary an out-of-plane anisotropy field H_k. The finite width of the strip lifts the degeneracy of standing-wave modes along the width w. To account for this, the in-plane wave vector $k_\parallel$ in Eq. (1) is written as $k_\parallel^2=k_x^2+\frac{n^2\pi^2}{w^2}$, where k_x is the propagation wave vector along the strip and n is an odd integer ($n=1,3,\ldots$) corresponding to the number of half wavelengths for the magnetostatic potential within the width (in the following, we will restrict the study to the lowest-lying mode $n=1$).

The damping is taken into account by adding a Gilbert term in the equation of motion of the magnetization, which results in the following substitution:[31]

$$\omega_H \rightarrow \omega_H + i\alpha\omega. \qquad (2)$$

For the case of a uniform precession in an infinite medium (purely circular precession), this translates into a frequency-sweep linewidth (FWHM) $\Delta\omega=2\alpha\omega$ and an exponential time decay $\tau=1/\alpha\omega$. In the case of MsFVW, the contribution to the FWHM is the same, but the resonance peaks are also broadened because of the spectral width of the excitation (see below).

B. Self-inductance measurements

Figure 2(a) shows a typical measurement of the real and imaginary parts of the self-inductance ΔL_{11}. This spectrum was obtained on a $t=20$ nm, $w=2$ μm, $\lambda=800$ nm, and $D=7.8$ μm sample [the one of Fig. 1(a)] under an applied field $\mu_0 H_{ext}=1.047$ T. It displays clear features of a ferromagnetic resonance (FMR) response. One recognizes two peaks of Lorentzian shape for the absorption $\mathrm{Im}(\Delta L_{11})$: the main one at a frequency $f_M=5.762$ GHz and a secondary one at $f_S=5.282$ GHz. These two resonance peaks reflect the signature of the antenna as shown by the Fourier transform of the current density [see Fig. 1(c)]. The antenna couples not only to wavelengths matching with its main spatial periodicity, but it also couples, in a lower extent, to lower wave vectors at lower frequencies that correspond to the secondary peak of $\tilde{j}_\epsilon(k)$.

Note that the base line of the signal is not zero. This is attributed to a slight variation of the antennae's impedance with the applied magnetic field, which differs from one sample to another and for which we do not have any clear explanation. Consequently, the subtraction of the two measurements taken at different but closely applied fields (reference and resonance) results in a base line that is either positive or negative, depending on whether the reference field is greater or smaller than the resonant field. One also notices that the two absorption spectra of each antenna, $\mathrm{Im}(\Delta L_{11})$ (red curve) and $\mathrm{Im}(\Delta L_{22})$ (magenta curve), are not completely identical. This illustrates the difficulties we have to obtain two identical devices even though they were made at the same time and are only a few μm apart from each other. The film was probably altered during the microfabrication process, which could explain a slight difference of the ferromagnetic response between the two antennae.

The plots of Figs. 2(c) and 2(d) sum up the self-inductance measurements performed over the frequency range [1–15 GHz] and constitute the ferromagnetic resonance characterization of the Permalloy strip. Figure 2(c) shows the magnetic field dependency of the resonance frequency of the two main peaks. From this plot and from the MsFVW dispersion relation (1), one derives the gyromagnetic ratio $\gamma/2\pi=30$ GHz T^{-1} (corresponding to a g factor $g=2.14$) and the effective magnetization $\mu_0 M_{eff}=0.88$ T ($M_{eff}=M_s-H_k$, where H_k is an out-of-plane anisotropy field). Figure 2(d) shows the frequency dependence of the FWHM of the absorption peak. In a PSWS experiment, the FWHM results on one hand from the intrinsic contribution of the damping due to the absorption $[(\Delta\omega)_{intrinsic}=2\alpha\omega$ in a perpendicularly magnetized film] and on the other hand, from the extrinsic contribution of the spectral width due to a nonperfectly monochromatic excitation: $(\Delta\omega)_{extrinsic}=v_g\Delta k$, where $v_g=d\omega/dk_x$ is the group velocity and Δk is the FWHM of the square of the Fourier transform of the current [see Fig. 1(c)]. Assuming that these two contributions can simply be added to one another, one writes

$$\Delta\omega \simeq 2\alpha\omega + v_g\Delta k. \qquad (3)$$

Deriving the dispersion relation (1) in the small wave-vector limit, one finds that the group velocity does not vary significantly as a function of the frequency ($v_g \simeq \omega_M \frac{t}{4}\frac{1}{\sqrt{1+\pi^2/k^2w^2}}$ as soon as the applied field exceeds the saturation field by a few percent), so that the damping factor can be extracted from the slope of the FWHM vs frequency: $\alpha=0.011$ for the plot shown in Fig. 2(d).

In this measurement mode which involves only one antenna, our technique can be seen as a special realization of broad-band inductive measurement of FMR. Such measure-

ments are typically carried out using coplanar waveguide with much larger dimensions (from tens of micrometers to a millimeter), a small piece of ferromagnetic film being directly laid onto the waveguide. The method is usually referred to as VNA-FMR, coplanar waveguide ferromagnetic resonance (CPW-FMR), or pulse-induced magnetometry (PIMM) when carried out in the time domain. Several examples of the use of these techniques can be found in Ref. 32–36. As noted,[37] such measurements involve the production of spin waves with a finite range of wave vectors, which lead to an increase of the linewidth compared to the intrinsic damping contribution. The distinguishing feature of PSWS is its ability to directly observe the propagation of these spin waves with the help of a second antenna as explained below.

C. Mutual inductance measurements

Figure 2(b) shows a typical mutual-inductance spectrum ΔL_{12}. It was measured in the same run as the self-inductance curves shown in panel (a). The real and imaginary parts of ΔL_{12} exhibit clear oscillations with a 90° phase lag. The amplitude of the oscillations is reminiscent of the two absorption peaks of the self-inductance. These oscillations are attributed to the phase delay accumulated by the spin waves during the propagation.

Let us put the intrinsic damping to the side for the moment ($\alpha=0$). Then, the wave vector of the spin waves is uniquely defined by the microwave angular frequency ω through the spin-wave dispersion (1). The oscillating magnetization in the spin wave takes the form of a plane wave: $\mathbf{m}(x,t)=\mathbf{m}_0 e^{i(wt-kx)}$. Let us now assume each antenna to be pointlike (i.e., its extension along the propagation direction $\mathcal{E}=0$). The phase delay for a transmission between the two antennae (distance D) is therefore $\phi=-kD$. Now, when the frequency is swept around the resonance, different wave vectors are selected according to the dispersion relation (1) and within the bandwidth of the $\tilde{j}_e(k)$ peak. Consequently, the phase delay varies continuously, giving rise to the oscillations seen in Fig. 2(b).

From the period f_p of the oscillations, we can estimate the group velocity v_g. In fact, for a full period, $\delta\phi=2\pi$. Assuming a constant group velocity within the wave-vector range of the main peak, we have $\delta k \simeq 2\pi f_p / v_g$. So the group velocity is equal to $v_g \simeq f_p . D$. Following this reasoning, we find for the experimental condition of Fig. 2(b) a group velocity $v_g=770$ m s^{-1}, which is slightly greater than the theoretical value 650 m s^{-1} obtained from differentiating Eq. (1).

In the same spirit, the attenuation of the spin wave can be estimated by comparing the amplitude of the mutual inductance to that of the self-inductance. In a continuous-wave experiment, the intrinsic damping manifests itself as a spatial decay of the oscillating magnetization within the spin wave which can be written $\mathbf{m}(x,t)=\mathbf{m}_0\, e^{-x/L_{att}} e^{i(wt-kx)}$, where L_{att} is the attenuation length over which the precession angle decays as $1/e$. The quantity $1/L_{att}$ can be seen as an imaginary part of the wave vector.[31] It is obtained by performing the substitution (2) in the dispersion relation of the spin wave. It appears as the spatial counterpart of the decay rate $1/\tau$, both quantities being related by the group velocity: $L_{att}=v_g\tau$. Assuming again that the wave vector is uniquely determined by the microwave frequency and that the two antennae are pointlike, the amplitude decay corresponding to the propagation between the two antennae is $\exp(-D/L_{att})$. Experimentally, this decay can be estimated as the ratio $2|\Delta L_{21}|/|\Delta L_{11}|$ (the factor 2 accounts for the fact that spin waves are being emitted in both directions $x>0$ and $x<0$). From this estimate, one obtains an experimental value $L_{att}=2.8$ μm which is larger than the theoretical one $L_{att}^{theo}=v_g/\alpha\omega=1.7$ μm.

The limitations of the discussion above are obvious. In the samples used in this study, the extension $\mathcal{E}$ of the antenna along the ferromagnetic strip [$\mathcal{E}\simeq 5$ μm for the antennae of Fig. 1(a)] is comparable to both the attenuation length ($L_{att} \simeq 2$ μm) and their center to center spacing $D\simeq 8$ μm [see Fig. 1(b)]. This invalidates the assumption of pointlike emitters and receivers. To be more explicit, let us consider the mutual inductance ΔL_{21} corresponding to spin waves propagating from left to right. Because the spin waves are significantly attenuated during their propagation below one antenna ($\mathcal{E}>L_{att}$), the signal is expected to be dominated by waves emitted in the right most meanders of the left antenna and received in the left-most meanders of the right antenna. One cannot assume either that the wave vector is selected strictly by the microwave angular frequency ω through the dispersion relation (1). Indeed, the linewidth introduced by the damping is larger than the linewidth introduced by the wave-vector spreading Δk of the excitation: $1/\tau > v_g \Delta k$. Noticing that the k spreading is inversely proportional to the lateral extension of the antenna ($\Delta k \simeq 1/\mathcal{E}$), one again obtains the same inequality $\mathcal{E}>L_{att}$.

This situation is typical of a miniaturized PSWS experiment on metal films. Because the inductive signal is small, it is desirable to work with antenna covering a relatively large portion of the ferromagnetic sample and situated close enough to each other. One can easily convince oneself that the signal is maximized when both the antenna extension and their spacing are of the order of the attenuation length. This is in strong contrast with older implementation of PSWS on YIG films. In this case, the very low microwave losses allow one to put the antenna far apart from each other, each antenna being a simple microstrip (typically $\mathcal{E}$ of the order of 100 μm, D and L_{att}=a few mms). The next section describes a calculation method which precisely describes the situation we are interested in. The coupling of the spin waves to the antennae is described with the help of a full electromagnetic calculation based on the determination of the magnetostatic potential in the reciprocal space. The intrinsic damping is introduced in a consistent way and all the parameters of PSWS (self- and mutual inductances) are calculated.

IV. MODEL

We now move on to the establishment of a model for spin-wave transduction. Contrary to recent reports,[16] we have chosen not to fully use numerical micromagnetic simulations because we wanted to highlight the physical processes governing the amplitude and shape of the PSWS signals. Following the early calculations of PSWS,[18–25] we shall

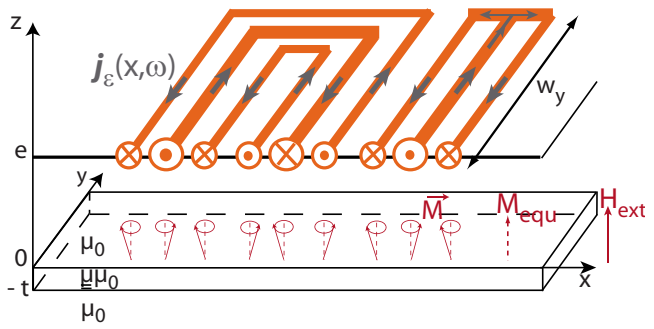

FIG. 3. (Color online) Sketch of one antenna and of the geometry considered for the electromagnetism calculation.

solve the problem for a Fourier component and use Fourier transforms to calculate the measurable quantities. The main difficulty of such calculations is to relate the magnetic quantities describing the spin wave (oscillating magnetization components or magnetostatic potential) to the electrical quantities describing the microwave signal in the antenna (microwave current and voltage). For this purpose, several methods have been proposed. Ganguly and Webb[19] and Vashkovskii *et al.*[21] calculated all the components of the electromagnetic fields in the layered medium consisting of the magnetic film, the dielectric media, and the metal of the antenna. Stancil[18] and Kalinikos[22] resolved the microwave signals onto the basis set formed by the spin-wave modes of the films. Finally, Emtage[20] proposed to use an intermediate quantity called surface permeability. This allows one to express the boundary conditions and the microwave signals in a compact form. We adapt this formalism by including the intrinsic damping and deriving expressions for both the self- and mutual inductances.[41]

A. Description of the problem

A sketch of the geometry of the problem is shown in Fig. 3. The antenna lays at height e above the ferromagnetic film of thickness t. For simplification, we assume the antenna is infinitely thin (current sheet), so that we work with a linear current density $j_\epsilon(x\omega)$. This is the main assumption of the calculation; in reality, the antenna thickness is about 150 nm. This is much smaller than the wavelength of the spin wave (0.8–1.6 μm) but larger than the spacer thickness or the magnetic film thickness. Without assuming this simplification, the calculation would be far too complicated and we will see that this assumption leads to some renormalization of the amplitude which can be easily dealt with. We also assume that the antenna is infinitely extended along the y coordinate (no dependence on y), so that we work with an inductance per unit length $\mathcal{L}$ ($\mathcal{L}=L/w_y$, where L is the inductance and w_y is the extension of the strip and of the antenna along y). The permeability tensor is considered to be $\mu_0\underline{\underline{1}}$ everywhere except for inside the ferromagnetic film where it is written as $\mu_0\underline{\underline{\mu}}$, where $\underline{\underline{\mu}}$ is a generic relative permeability tensor accounting for the gyromagnetic response of the magnetic material (see the next sections).

Let us start by expressing the self-inductance of the excitation antenna in term of the total complex power P_{tot},

$$L_{11}(\omega) = w_y \mathcal{L}_{11}(\omega) = \frac{P_{tot}}{i\omega I^2} = \frac{w_y}{i\omega I^2}\int dx E_y(x,e,\omega) j_\epsilon(x,\omega), \tag{4}$$

where $E_y(x,e,\omega)$ is the electrical field induced on the plane of the antenna. According to the theorem of Parseval, "the total energy contained in a waveform does not depend on its representation." We can rewrite the integration (4) in the reciprocal space

$$\mathcal{L}_{11}(\omega) = \frac{1}{i2\pi\omega I^2}\int_{-\infty}^{+\infty} dk \tilde{E}_y(k,e,\omega)\tilde{j}_\epsilon(k,\omega), \tag{5}$$

where $\tilde{E}_y(k,e,\omega)$ and $\tilde{j}_\epsilon(k,\omega)$ are, respectively, the Fourier transform of the electrical field on the antennae $E_y(x,e,\omega)$ and of the linear current density $j_\epsilon(x,\omega)$. When considering the spin-wave transduction from antenna 1 to antenna 2, we simply write the mutual inductance $\mathcal{L}_{21}$ by factoring a phase delay term e^{-ikD} in the integrand of Eq. (5)

$$\mathcal{L}_{21}(\omega) = \frac{1}{i2\pi\omega I^2}\int_{0}^{+\infty} dk \tilde{E}_y(k,e,\omega)\tilde{j}_\epsilon(k,\omega)e^{-ikD}. \tag{6}$$

This accounts for the fact that the excitation signal $[j_\epsilon(x,\omega)]$ and the reception signal $[E_y(x,e,\omega)]$ are shifted by an amount D on the x scale. The integration for the mutual inductance is limited to positive k only, since spin waves traveling toward negative x values are not detected by the second antenna.

Remembering that the Fourier transform of the current distribution $\tilde{j}_\epsilon(k,\omega)$ is the subject of the Appendix, we now have to solve the problem for each of the Fourier components, i.e., be given a harmonic distribution of current $\tilde{j}_\epsilon(k,\omega)e^{i(\omega t-kx)}$ to calculate the electric field $\tilde{E}_y(k,z,\omega)e^{i(\omega t-kx)}$ induced by the magnetic response of the dielectric media and ferromagnetic film. This problem is sketched in Fig. 4. Let us now express both the current and electrical fields in terms of magnetic quantities:

(i) Applying the Ampere theorem to a little contour extending across the plane in which the current flows (see the rectangle in Fig. 4), we arrive at

$$\tilde{h}_x(k,e^+,\omega) - \tilde{h}_x(k,e^-,\omega) = \tilde{j}_\epsilon(k,\omega), \tag{7}$$

which expresses that the current drives a jump of the tangential component of the magnetic field across the plane in which it flows.

(ii) Writing "Maxwell-Ampere" equation ($\nabla\times\mathbf{E}=-\frac{d\mathbf{b}}{dt}$) for the wave forms given above, we directly obtain

$$\tilde{E}_y(k,z,\omega) = -\frac{\omega}{k}\tilde{b}_z(k,z,\omega), \tag{8}$$

which expresses that the electrical field is generated by the time-varying magnetic flux. Note that it comprises both the signal induced by the spin wave and the signal induced by direct electromagnetic coupling of the current distribution onto itself. Equations (7) and (8) bring us to a purely magnetic problem consisting in solving for the magnetic fields and magnetization profiles through the thickness of the stack.

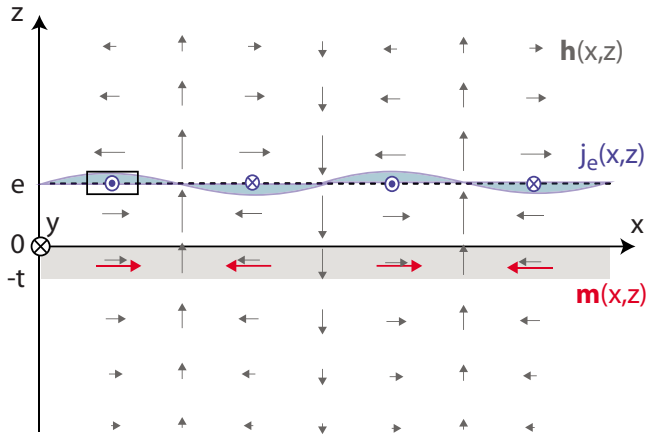

FIG. 4. (Color online) Vector field distribution of the magnetostatic field **h** for a given Fourier component of wave vector k. The distributions of the linear current density $\mathbf{j}_\epsilon$ and oscillating magnetization **m** are sketched as arrows. The magnetostatic field was calculated for the following set of parameters: $kt=0.16$, $ke=0.32$, $H_{equ}/M_s=0.2$, and $\omega \ll \gamma\mu_0 H_{equ}$ (i.e., far below resonance).

We shall now describe the gyromagnetic response of the film before we solve this problem.

B. Gyromagnetic response of the film

The time evolution of the magnetization **M** is described by the Landau-Lifshitz-Gilbert equation[31]

$$\frac{d\mathbf{M}}{dt} = \gamma\mu_0 \mathbf{H}_{eff} \times \mathbf{M} + \alpha \frac{\mathbf{M}}{M_s} \times \frac{d\mathbf{M}}{dt}, \tag{9}$$

where H_{eff} is an effective field comprising all the magnetic interactions in the system. In the case of small amplitude harmonic oscillations around the equilibrium, we introduce a coordinate axis system (x_1,x_2,x_3) adapted to the equilibrium direction $\mathbf{M}_{equ}$, which is set along x_3. In this coordinate system, the magnetization and magnetic field write:

$$\mathbf{M} = \begin{pmatrix} m_1 e^{i\omega t} \\ m_2 e^{i\omega t} \\ M_{equ} \end{pmatrix} \quad \text{and} \quad \mathbf{H}_{eff} = \begin{pmatrix} h_1 e^{i\omega t} \\ h_2 e^{i\omega t} \\ H_{equ} \end{pmatrix},$$

with $m_1, m_2 \ll M_{equ}$ and $h_1, h_2 \ll H_{equ}$. Then, Eq. (9) is linearized as follows:

$$i\omega\mathbf{m} = \gamma\mu_0(\mathbf{H}_{equ} \times \mathbf{m} + \mathbf{h} \times \mathbf{M}_{equ}) + \alpha \frac{\mathbf{M}_{equ}}{\mathbf{M}_s} \times i\omega\mathbf{m}, \tag{10}$$

where H_{equ} is the equilibrium field already defined in Sec. III A.

After projecting Eq. (10) in the $\{x_1,x_2\}$ plane, we obtain $\mathbf{m}=\underline{\chi}\mathbf{h}$, which expresses the linear relationship between the oscillating magnetization and the oscillating effective field. Here, $\underline{\chi}$ is the Polder susceptibility tensor, whose components write

$$\chi_{11} = \chi_{22} = \chi = \frac{\omega_M \omega_H}{\omega_H^2 - \omega^2}; \quad \chi_{21} = -\chi_{12} = i\kappa = i\frac{\omega_M \omega}{\omega_H^2 - \omega^2}, \tag{11}$$

with $\omega_M = \gamma\mu_0 M_s$ and $\omega_H = \gamma\mu_0 H_{equ} + i\alpha\omega$ as defined in Sec. III A.

Note that in the following, we shall solve the magnetostatic field using a generic permeability tensor μ defined in the coordinate system adapted to the antenna, so that the expressions can be applied to any spin-wave geometry:

$$\underline{\mu} = \mu_0 \begin{pmatrix} \mu_{xx} & \mu_{xz} \\ \mu_{zx} & \mu_{zz} \end{pmatrix}.$$

The relation between this tensor and the Polder susceptibility depends on the orientation of the equilibrium magnetization with respect to the antenna. For the geometry addressed in the paper (M_{equ} out of the film plane, i.e., the so-called magnetostatic forward volume wave configuration), the axis (x_1,x_2,x_3) can be identified to (x,y,z), so that

$$\mu_{xx} = 1 + \chi, \quad \mu_{zz} = 1 \quad \mu_{xz} = \mu_{zx} = 0. \tag{12}$$

C. Magnetostatic problem

For the range of wavelengths that are excited ($\lambda \simeq 800$ nm $\gg l_{ech} \simeq 5$ nm), we can ignore the contribution of the exchange field in the effective field of Eq. (10). The oscillating effective field h can therefore be identified to a purely magnetostatic field. It comprises both the field produced by the current flowing through the antenna and the dipole field produced by the magnetization in the spin wave. The absence of electrical current in both half spaces, above and below the antenna, implies that $\nabla \times \mathbf{h} = 0$. This allows one to describe the magnetic system with a scalar potential $\psi(x,z,t)$ (reminded that there is no dependence on coordinate y), such that $\mathbf{h}(x,z,t) = -\nabla\psi(x,z,t)$. Owing to the geometry of the problem (harmonic distribution along the x axis), the magnetostatic potential $\psi(x,z,t)$ must have the form of a propagating wave along the x coordinate. The dependence along the z coordinate is deduced from the condition of zero divergence $\nabla \cdot \mathbf{b} = -\nabla \cdot \underline{\mu} \nabla \psi = 0$ (Walker equation). As a consequence, the magnetostatic potential writes as

$$\psi(x,z,t) = (Ae^{-iqz} + Be^{iqz})e^{i(wt-kx)}, \tag{13}$$

where $q = i\beta k$, with $\beta = \frac{\mu_{xx}}{\mu_{zz}}$ ($q = ik$ in the dielectric media). The constants A and B are obtained by solving the boundary conditions of the problem.

Instead of solving directly for the magnetostatic potential and fields, we introduce, as in the initial formulation of Emtage,[20] a dimensionless quantity $\mu_s(k,z,\omega)$ called the surface permeability, which is defined as the ratio of the transverse induction $b_z(k,z,\omega)$ (flux) to the pumping field $h_x(k,z,\omega)$ (excitation)

$$\mu_s(k,z_0,\omega) = \lim_{z \to z_0} -i\frac{\tilde{b}_z(k,z,\omega)}{\mu_0 \tilde{h}_x(k,z,\omega)}. \tag{14}$$

This quantity will be used to write in a compact way (i) a solution of the magnetostatic equations in a given medium,

(ii) continuity relations at the boundary between two media, and (iii) the discontinuity at the current-carrying surface. Let us write these relations:

(i) Using the magnetostatic potential defined by Eq. (13) and the generic permeability tensor $\underline{\underline{\mu}}=\mu_0\begin{pmatrix}\mu_{xx} & \mu_{xz}\\ \mu_{zx} & \mu_{zz}\end{pmatrix}$, one can eliminate the constants A and B to derive a relation between the surface permeabilities $\mu_s(z_1)$ and $\mu_s(z_2)$ at two different positions in the same medium

$$\mu_s(z_2)=\frac{\mu_s(z_1)+[\beta^2\mu_{zz}^2+\mu_{zx}^2-i\mu_s(z_1)\mu_{zx}]\frac{\tanh[\beta k(z_1-z_2)]}{\beta\mu_{zz}}}{1+[\mu_s(z_1)+i\mu_{zx}]\frac{\tanh[\beta k(z_1-z_2)]}{\beta\mu_{zz}}}. \tag{15}$$

This relation can be applied to the dielectric media ($\underline{\underline{\mu}}=\mu_0\underline{\underline{1}}$), but also to the ferromagnetic medium (using the permeability tensor given in the last section).

In the two dielectric half spaces extending to infinity ($z<-t$ and $z>e$), the surface permeability takes a particularly simple form. From Eq. (13), the requirement that $\psi(x,z,\omega)$ does not diverge implies the vanishing of A (respectively, B) for the half space extending toward $z\to+\infty$ (respectively, $z\to-\infty$). The magnetostatic potential therefore writes as an evanescent wave decaying away from the system: $\psi(x,\infty)\sim e^{-|kz|}e^{-ikx}$. The corresponding surface permeability is simply $\mu_s(k,\pm\infty)=\mp|k|/k=\mp\mathrm{sgn}(k)$ and its sign depends on the propagation direction.

(ii) The electromagnetic interface relations imply that the surface permeability is continuous across a boundary that does not carry a current. This allows one to iterate relation (15). From $\mu_s(k,-t,\omega)=\mu_s(k,-\infty)$, one can express $\mu_s(k,0,\omega)$ using Eq. (15) with the permeability of the magnetic film and from $\mu_s(k,0,\omega)$, one can deduce $\mu_s(k,e^-,\omega)$ using the permeability of the dielectric medium.

(iii) The magnetic field discontinuity across the antenna described by Eq. (7) is simply rewritten using the upper limit $\mu_s(k,e^+,\omega)$ and lower limit $\mu_s(k,e^-,\omega)$ of the surface permeability

$$\mu_0\tilde{j}_\epsilon(k,e,\omega)=-i\tilde{b}_z(k,e,\omega)\left(\frac{1}{\mu_s(k,e^+,\omega)}-\frac{1}{\mu_s(k,e^-,\omega)}\right). \tag{16}$$

Here, $\mu_s(k,e^-,\omega)$ is obtained by iteration as indicated above and $\mu_s(k,e^+,\omega)=\mu_s(k,+\infty)$. The complicated vector distribution of the magnetic field and magnetic induction across the layered structure shown in Fig. 4 is therefore replaced by simple scalar relations for the surface permeability.

Finally, by combining the Eqs. (8) and (16), we can re-express the electrical field in terms of the Fourier transform of the current density and of the surface permeabilities (which only depends on the geometry of the system and on the magnetic parameter of the ferromagnetic film)

$$\tilde{E}_y(k,e,\omega)=i\mu_0\frac{\omega}{k}\frac{\tilde{j}_\epsilon(k,\omega)}{\frac{1}{\mu_s(k,e^+,\omega)}-\frac{1}{\mu_s(k,e^-,\omega)}}. \tag{17}$$

Inserting Eq. (17) into the integrals (5) and (6), we obtain the expressions of the self-inductance and mutual inductance per unit length that will be integrated numerically

$$\mathcal{L}_{11}=\frac{\mu_0}{2\pi}\int_{-\infty}^{+\infty}dk\frac{1}{k}\left|\frac{\tilde{j}_\epsilon(k,\omega)}{I}\right|^2\frac{1}{\frac{1}{\mu_s(k,e^+,\omega)}-\frac{1}{\mu_s(k,e^-,\omega)}},$$

$$\mathcal{L}_{21}=\frac{\mu_0}{2\pi}\int_{0}^{+\infty}dk\frac{e^{-ikD}}{k}\left|\frac{\tilde{j}_\epsilon(k,\omega)}{I}\right|^2\frac{1}{\frac{1}{\mu_s(k,e^+,\omega)}-\frac{1}{\mu_s(k,e^-,\omega)}}. \tag{18}$$

After integration, the total inductances of the antenna are obtained by multiplying the result with the width w of the strip.

D. Physical interpretation

From expressions (18), the factors governing the PSWS signal appear clearly. For obtaining the self-inductance, the gyromagnetic response contained in the term $\mu_s(k,e^-,\omega)$ is multiplied by the Fourier transform of the antenna current, which explains why the total width is a convolution of the width of those two factors. One would recover a width entirely given by the gyromagnetic response if the antenna was made perfectly monochromatic (an antenna consisting of an infinite number of meanders). On the other hand, one would recover a width entirely given by the shape of the antenna if the film had vanishing loss (a situation well recognized in the case of YIG films).

As far as the mutual inductance is concerned, the situation is a little bit more subtle because the two factors mentioned above are again multiplied with an oscillation (e^{-ikD}). It is clear that the integral will decrease when the number of oscillations within the width of the nonoscillating terms increases. This is the way the attenuation appears in that calculation: because of the finite linewidth of the gyromagnetic response, spin waves with a finite range of wave vectors are produced at the same time. During their propagation, these waves interfere with each other. The signal decreases as a function of the antenna to antenna distance (because this sets the period of the oscillation in the integrand) and as a function of the linewidth of the gyromagnetic response (because this sets the range over which the oscillation is integrated).

To provide a deeper understanding of this calculation, the different terms of the integrand of Eq. (18) are represented in Fig. 5. We separately plot the current distribution $|\tilde{j}_\epsilon(k)/I_0|^2$ which set the emission spectra, the gyromagnetic response term $L_{equ}(k,\omega)=\mu_0\frac{1}{\frac{1}{\mu_s(k,e^+,\omega)}-\frac{1}{\mu_s(k,e^-,\omega)}}$ (Ref. 42) for a frequency equal to the MsFVW frequency at the wave vector k_M, and the real part of the oscillating term e^{-ikD} that corresponds to the spin-wave propagation. Once again, the resulting mutual-inductance spectrum L_{21} is obtained by integrating the product of these three terms.

Note that this model can be implemented the same way for the case of magnetostatic surface wave (MsSW: magnetization in the plane of the film and perpendicular to k) or magnetostatic backward volume wave (MsBVW: magnetization in plane parallel to k). The point is simply to insert the proper components of the Polder susceptibility tensor into

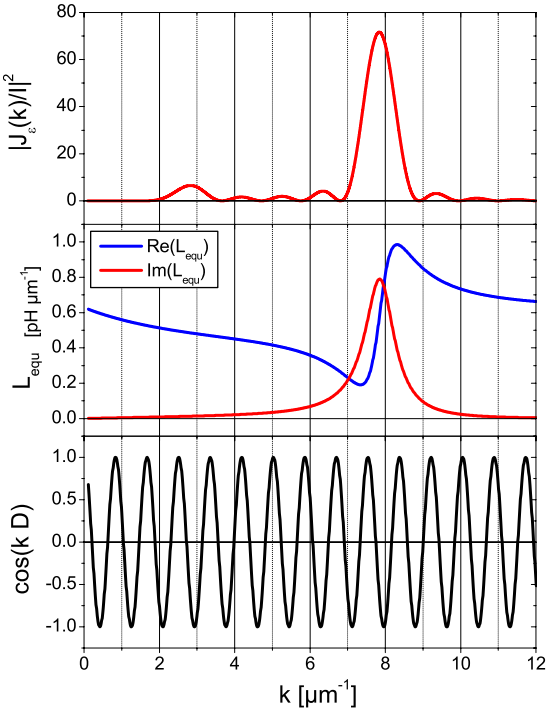

FIG. 5. (Color online) Plots of the three terms contained in the integrand of Eq. (18). (a) Normalized current distribution $|\tilde{j}(k)|^2$ for the antennae shown in Fig. 1(a). (b) Gyromagnetic response term $L_{equ}(k,\omega)$ calculated for a frequency $f=4.48$ GHz. The parameters are $\mu_0 H_{ext}=1.0$ T, $t=20$ nm, $h=160$ nm, $\gamma/2\pi=30$ GHz T^{-1}, and $\mu_0 M_s=0.88$ T. (c) Oscillating term for $D=7.5$ μm.

the generic permeability tensor $\underline{\underline{\mu}}$. The Polder susceptibility tensor is written in the plane perpendicular to the equilibrium magnetization [see Sec. IV B], while the spin-wave transduction problem $[\underline{\underline{\mu}}(x,z,t)]$ is calculated in the plane perpendicular to the antenna [see Fig. 3]. The generic permeability tensors, $\underline{\underline{\mu}}_{\mathrm{MsSW}}$ for case of surface waves and $\underline{\underline{\mu}}_{\mathrm{MsBVW}}$ for the case backward volume waves, writes as

$$\underline{\underline{\mu}}_{\mathrm{MsSW}} = \mu_0 \begin{pmatrix} 1+\chi & -i\kappa \\ i\kappa & 1+\chi \end{pmatrix} \quad \text{and} \quad \underline{\underline{\mu}}_{\mathrm{MsBVW}} = \begin{pmatrix} 1 & 0 \\ 0 & 1+\chi \end{pmatrix}.$$

V. COMPARISON TO EXPERIMENT

We report in Fig. 6 the comparison of the results of our model to several measured spectra obtained on four different samples. The simulated inductances L_{11} and L_{21} were calculated from the integral relations (18) using the magnetic parameters $(\gamma, M_{eff}, \alpha)$ derived from the FMR study for each strip [see Figs. 2(c) and 2(d)]. We set an average height e of 160 nm, which accounts for the 90 nm spacer thickness and half of the antenna thickness ($\simeq$70 nm). Offsets are added to the real and imaginary parts of the self-inductances. This accounts for the direct electromagnetic coupling [which results in a nonzero baseline for $\mathrm{Re}(\Delta L_{11})$] and for experimental uncertainties in determining the baseline (see the discussion in Sec. III B). The spectrum for a given set of experimental conditions is also multiplied by a scale factor c of the order of 0.65–0.9. This factor accounts for the fact that the spin-wave amplitude is not uniform along the width of the strip but rather sinusoidal with one antinode. This implies an overlap integral of $8/\pi^2 \approx 0.81$.[38] Subsequently, the average spacer thickness e and the amplitude correction factor c are finely adjusted for each spectra to obtain a better fit of the measurements, mainly to compensate for amplitude artifacts related to the assumption of an infinitely thin antenna (see the discussion below).

One can easily appreciate in the fits presented in Fig. 6 a good quantitative agreement between simulations and measurements. Within a few attempts playing reasonably with a few parameters, one finds no difficulties to have the simulated spectra pass through the measurement points. The simulations account correctly for the shape of the self-inductance: on all spectra, we noticed the presence of the two peaks. Both in measurements and simulations, these two peaks overlap more when the frequency is increased and for antenna producing smaller k. This is due to the interplay between the intrinsic damping (which broadens the peaks) and the Fourier transform of the antenna current (which sets the separation between the two peaks). The simulation also predicts the correct trends for the amplitude of the peaks: the amplitude increases when the width of the strip increases and also when the number of meanders of the antenna increases (because this increases the maximum amplitude of the Fourier transform of the current, see the Appendix).

Correct trends are also obtained as far as the mutual inductances are concerned even if this quantity appears to be more dependent on the precise values of the parameters: one observes a correct period and phasing for the oscillations. One also observes that the amplitude ratio between the low-frequency oscillations and the high-frequency ones seen for the mutual inductance is larger than the amplitude ratio between the low-frequency peak and the high-frequency one in the self-inductance signals. This is because the attenuation rate increases linearly as a function of frequency, so that low-frequency spin waves propagate further away. Interestingly, the simulation also reproduces a trend which is more difficult to explain from intuition: on Fig. 6(b), one clearly recognizes two peaks in the self-inductance spectrum but the two oscillation packets seem to merge with each other in the mutual-inductance spectrum.

Let us now discuss the limitations of this calculation. The main problem is related to the assumption of an infinitely thin antenna. In fact, recalling the form of the magnetostatic potential $\psi(\mathbf{r},t) \sim e^{-kz} e^{i(wt-kx)}$ Eq. (13), it is clear that the part of the current flowing in the top of the antenna is less strongly coupled to the spin waves than the part of the current flowing in the bottom of the antenna. Assuming the current to flow entirely in the midplane of the antenna will somehow underestimate the intensity. From the form of the magnetostatic potential, it is clear that this effect will be stronger for higher wave vectors. One can also convince oneself that this effect does not affect the self-inductance and the mutual inductance in an identical way.

To compensate for these artifacts, we have chosen to separately adjust the parameter e and the global scale factor c. Fortunately, these parameters need only to be adjusted

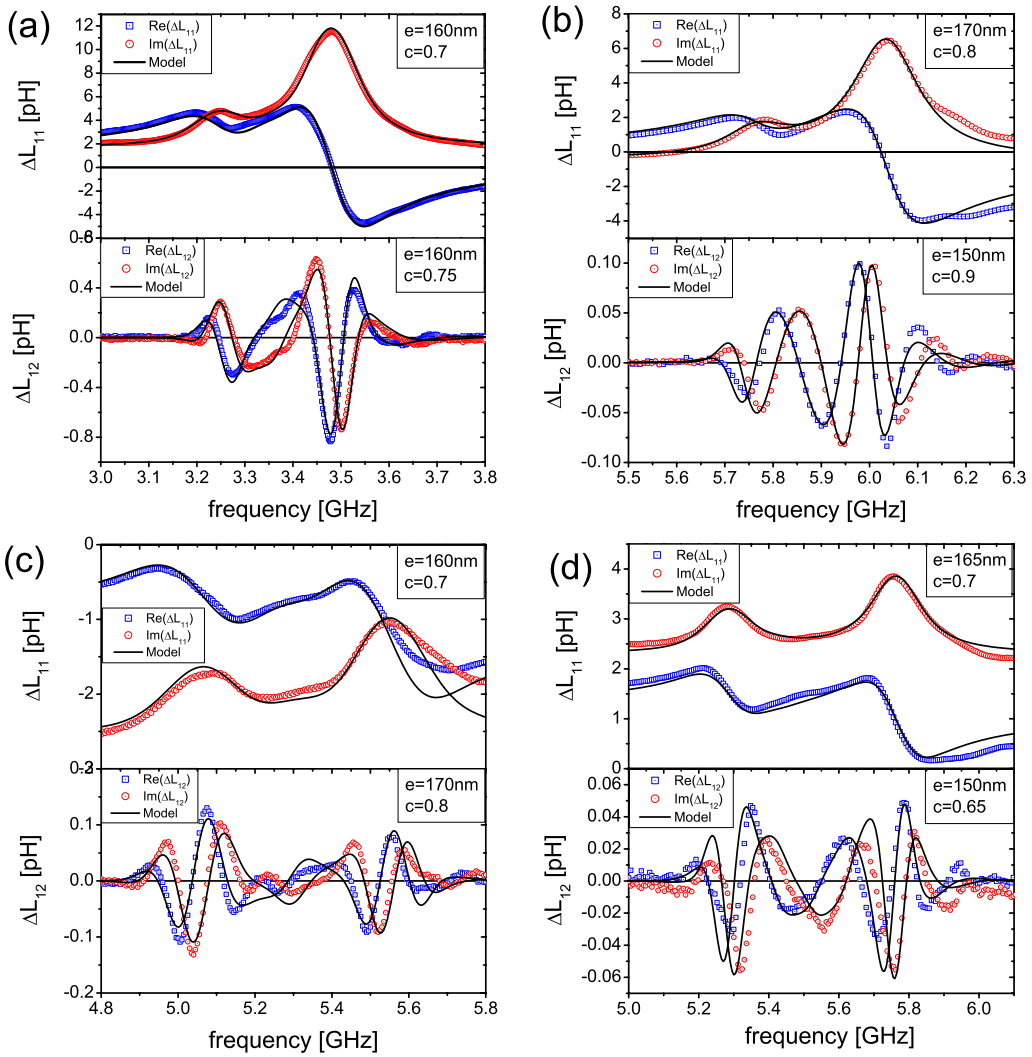

FIG. 6. (Color online) Comparison between simulation and measurements for four different samples. All samples have a nominal Permalloy film thickness $t=20$ nm, an effective magnetization $\mu_0 M_{eff}=0.88$ T, and gyromagnetic ratio $\gamma 2\pi=30$ GHz T^{-1}. The anisotropy field is taken equal to zero. (a) Spectra obtained on a $\lambda=1.6$ μm pair of antennae (three meanders) distant of $D=8.8$ μm and coupled with $w=7.8$ μm Permalloy strip under an external field $\mu_0 H_{ext}=0.983$ T. For the simulation, the thickness is adjusted to $t=17$ nm and the damping parameter is $\alpha=0.014$. (b) Same for $\lambda=1.6$ μm (five meanders), $D=14.5$ μm, $w=3.5$ μm, $\mu_0 H_{ext}=1.067$ T, $t=17.5$ nm, and $\alpha=0.012$. (c) Same for $\lambda=800$ nm (three meanders), $D=5.5$ μm, $w=3.5$ μm, $\mu_0 H_{ext}=1,037$ T, $t=19$ nm, and $\alpha=0.013$. (d) Same for $\lambda=800$ nm (five meanders), $D=7.7$ μm, $w=2$ μm, $\mu_0 H_{ext}=1.036$ T, $t=18.5$ nm, and $\alpha=0.012$.

over a range of about 10% to reach a good agreement (see the values on the plot of Fig. 6). Note that if these parameters were fixed to the nominal values ($e=160$ nm, $c=0.81$), we would still reach a good qualitative agreement, with reasonable errors of the order of 20% of the amplitude.[43]

Even after fine tuning these parameters, some little imperfections still remain in the shape of the oscillations. They can be attributed to the slight difference in the magnetic coupling of the two antennae. As seen in Fig. 2(a), the self-inductance spectra of the two antennae are always slightly different. Since the transmission signal contains the convolution of the magnetic responses of each antenna, a difference between ΔL_{11}'s and ΔL_{22}'s intensities or resonance frequencies leads to some deviations with the model that considers a perfect translation of one antenna. Another reason for these deviations could be a variation of the temperature during the scan. The spectra result from the averaging of several scans during hours over which the temperature cannot be maintained perfectly constant. The resultant drift of the resonance frequency can lead to a decrease of the intensity of the oscillations seen in the mutual inductance.

VI. CONCLUSION

We presented measurements of propagating spin-wave spectroscopy conducted on Permalloy strips at a submicrometer scale. These experiments can be interpreted using simple arguments of plane-wave propagation. However, such arguments do not allow one to precisely account for the measured spectra. For this purpose, we derive a calculation which relates the microwave response of the spin-wave antenna written in the reciprocal space to the gyromagnetic response of the magnetic film. Using this calculation method, one obtains a very good agreement with the measurements.

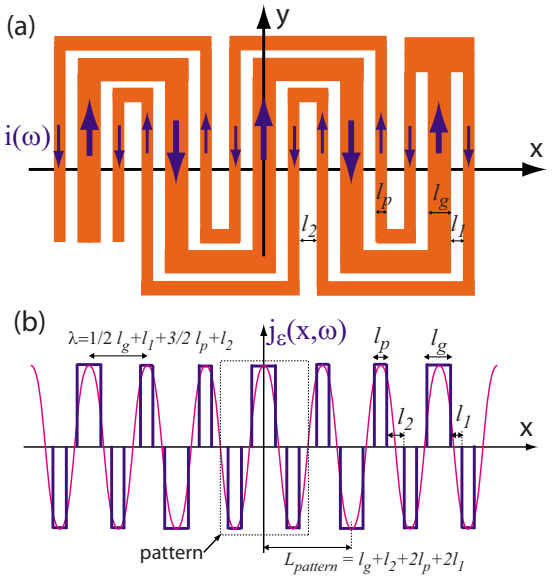

FIG. 7. (Color online) (a) Sketch of an antenna containing five meanders. (b) Current distribution $j_\epsilon(x,\omega)$ in the real space.

The spin-wave transduction calculation method described in this paper can be used for interpreting in detail propagating spin-wave spectra in various geometries. It could also be used in the context of coplanar waveguide broadband ferromagnetic resonance. Importantly, the calculation provides a very detailed understanding of the PSWS signal. We believe this to be a decisive point for future improvement of spin-wave experiments. High-efficiency miniature antenna could be used for micromagnetic studies,[3–5] for spin transfer experiments,[6,7,28,39] and also to investigate nonlinear effects because in that case, a large amplitude precession is easily obtained even with a very small microwave power.

ACKNOWLEDGMENTS

The authors would like to thank Julie Grolier and Cyril Deranlot (Unité Mixte CNRS/Thalès) for providing the Permalloy film, Arnaud Boulard for the fabrication of the measurement setup and the electromagnet, Yves Henry and Pierre Panissod for useful advice, and Alain Carvalho for the nice photographs of the setup. This work was supported by the ANR "Spectro-Spin" project.

APPENDIX: FOURIER TRANSFORM OF THE CURRENT DISTRIBUTION

For our spin-wave Doppler shift experiment based on the PSWS, we needed to work with high wave vectors as close as possible to a monochromatic excitation. For this reason, we chose the meander shape for the antennae. Furthermore, we adopted the geometry of a coplanar waveguide, a center conductor in between two ground conductors, so that it fits with the coaxial cable symmetry. We also designed the central track to be 2 times larger than the two ground tracks to ensure that a constant current density flows along the meander. And finally, we adjusted the distance between each pad to be as close as possible to a sinusoidal distribution.

A sketch of the current distribution for a typical antenna is shown in Fig. 7. We can resolve such a distribution by considering an elementary pattern containing the central conductor with its two neighboring ground tracks. This pattern is repeated 4 times away from the center and successively weighted by −1 and +1. The Fourier transform of the linear current density of this elementary pattern normalized by the total current I is written as

$$\frac{\tilde{j}_{pattern}(k)}{I} = \frac{\sin(kl_g/2)}{kl_g/2} - \cos[k(l_g + l_p + 2l_1)/2]\frac{\sin(kl_p/2)}{kl_p/2}, \tag{A1}$$

where the lengths l_g, l_p, and l_1 are defined in the sketch of the current distribution in Fig. 7. The pattern being translated the first time by $+L_{motif}$ and $-L_{motif}$ with a factor −1 and the second time by +2 L_{motif} and −2 L_{motif} with a factor +1, the complete Fourier transform of the linear current density takes the following form:

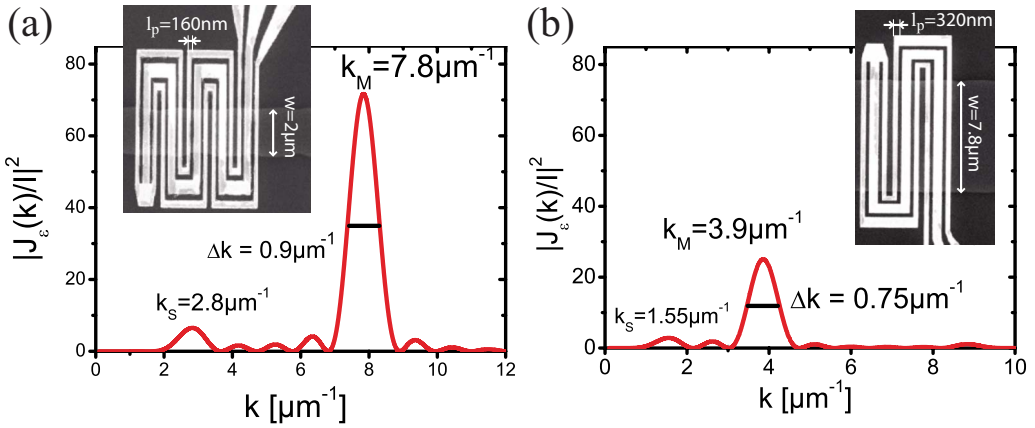

FIG. 8. (Color online) Fourier transform of the current distribution $\tilde{j}_\epsilon(k,\omega)$ for two different antennae. (a) An antenna with five meanders and with dimensions l_p=l_1=160 nm, l_g=320 nm, and l_2=240 nm. (b) An antenna with three meanders and with dimensions l_p=l_1=320 nm, l_g=640 nm, and l_2=480 nm.

$$\frac{\tilde{j}_\epsilon(k)}{I} = \frac{\tilde{j}_{pattern}(k)}{I}[1 - 2\cos(kL_{motif}) + 2\cos(2kL_{motif})]. \quad \text{(A2)}$$

The integral expressions of the inductance Eq. (18) bring the term $|\frac{\tilde{j}_\epsilon(k)}{I}|^2$ into play, so we plot in Fig. 8 the square of the Fourier transform normalized by the total current for two different antennae. The first one [Fig. 8(a)] corresponds to an antenna with five meanders and with the following dimensions: $l_p=l_1=160$ nm, $l_g=320$ nm, and $l_2=240$ nm, and the second one [Fig. 8(b)] corresponds to an antenna with three meanders and with double dimensions $l_p=l_1=320$ nm, $l_g=640$ nm, and $l_2=480$ nm. These plots, which represent the spin-wave emission spectra of an antenna, show an excitation that is not perfectly monochromatic. Indeed, the emission spectra always display on top of the main peak, which corresponds to the periodicity of the meander, a secondary one at lower wave vectors which is about 10 times less intense. Furthermore, each of the peaks has a finite width. These two aspects acting against monochromaticity are both due to the geometry and the finite extension of the antenna. Finally, one also notices the difference of intensity between the main peak of the two spectra presented. The more meanders the antenna has, the closer it is to a monochromatic case and the sharper the emission spectra is. In addition to the two antennae presented in Fig. 8, we worked with two other designs varying the dimension and the extension, one with double dimensions and five meanders and the last one with normal size and three meanders.

*matthieu.bailleul@ipcms.u-strasbg.fr

[1] A. Khitun, M. Bao, and K. Wang, IEEE Trans. Magn. **44**, 2141 (2008).
[2] M. P. Kostylev, A. A. Serga, T. Schneider, B. Leven, and B. Hillebrands, Appl. Phys. Lett. **87**, 153501 (2005).
[3] R. Hertel, W. Wulfhekel, and J. Kirschner, Phys. Rev. Lett. **93**, 257202 (2004).
[4] S. Choi, K.-S. Lee, K. Y. Guslienko, and S.-K. Kim, Phys. Rev. Lett. **98**, 087205 (2007).
[5] D.-S. Han, S.-K. Kim, J.-Y. Lee, S. J. Hermsdoerfer, H. Schultheiss, B. Leven, and B. Hillebrands, Appl. Phys. Lett. **94**, 112502 (2009).
[6] Y. Le Maho, J.-V. Kim, and G. Tatara, Phys. Rev. B **79**, 174404 (2009).
[7] V. Vlaminck and M. Bailleul, Science **322**, 410 (2008).
[8] M. Bailleul, D. Olligs, C. Fermon, and S. O. Demokritov, Europhys. Lett. **56**, 741 (2001).
[9] M. Bailleul, D. Olligs, and C. Fermon, Appl. Phys. Lett. **83**, 972 (2003).
[10] P. K. Amiri, B. Rejaei, M. Vroubel, and Y. Zhuang, Appl. Phys. Lett. **91**, 062502 (2007).
[11] A. Kozhanov, D. Ouellette, Z. Griffith, M. Rodwell, A. P. Jacob, D. W. Lee, S. X. Wang, and S. J. Allen, Appl. Phys. Lett. **94**, 012505 (2009).
[12] S. Tamaru, J. A. Bain, R. J. M. van de Veerdonk, T. M. Crawford, M. Covington, and M. H. Kryder, Phys. Rev. B **70**, 104416 (2004).
[13] K. Perzlmaier, G. Woltersdorf, and C. H. Back, Phys. Rev. B **77**, 054425 (2008).
[14] V. E. Demidov, J. Jersch, S. O. Demokritov, K. Rott, P. Krzysteczko, and G. Reiss, Phys. Rev. B **79**, 054417 (2009).
[15] T. J. Silva, M. R. Pufall, and P. Kabos, J. Appl. Phys. **91**, 1066 (2002).
[16] M. Covington, T. M. Crawford, and G. J. Parker, Phys. Rev. Lett. **89**, 237202 (2002).
[17] Z. Liu, F. Giesen, X. Zhu, R. D. Sydora, and M. R. Freeman, Phys. Rev. Lett. **98**, 087201 (2007).
[18] D. D. Stancil, *Theory of Magnetostatic Waves* (Springer, New York, 1993).
[19] A. Ganguly and D. Webb, IEEE Trans. Microwave Theory Tech. **23**, 998 (1975).
[20] P. R. Emtage, J. Appl. Phys. **49**, 4475 (1978).
[21] A. Vashkovskii, S. Gerus, I. Dikshtein, and V. Tarasenko, Sov. Phys. Tech. Phys. **24**, 360 (1979).
[22] B. Kalinikos, *Spectrum and Linear Excitation of Spin Waves in Ferromagnetic Films* (Plenum Publishing Corporation, New York, 1982).
[23] P. R. Emtage, J. Appl. Phys. **53**, 5122 (1982).
[24] S. A. Bogacz and J. B. Ketterson, J. Appl. Phys. **58**, 1935 (1985).
[25] G. Vugalter, B. Gusev, A. Gurevich, and O. Chivileva, Sov. Phys. Tech. Phys. **31**, 87 (1986).
[26] L. K. Brundle and N. J. Freedman, Electron. Lett. **4**, 132 (1968).
[27] W. Ishak, Proc. IEEE **76**, 171 (1988).
[28] V. Vlaminck, Ph.D. thesis, Université Louis Pasteur, 2008; http://eprints-scd-ulp.u-strasbg.fr:8080/1053/
[29] S. Ramo, J. Whinnery, and T. Van Duzer, *Fields and Waves in Communication Electronics* (Wiley, New York, 1965).
[30] B. Kalinikos, IEE Proc., Part H: Microwaves, Opt. Antennas **127**, 4 (1980).
[31] A. Gurevich and G. Melkov, *Magnetization Oscillations and Waves* (CRC Press, Cleveland, 1996).
[32] Y. Ding, T. J. Klemmer, and T. M. Crawford, J. Appl. Phys. **96**, 2969 (2004).
[33] S. S. Kalarickal, P. Krivosik, M. Wu, C. E. Patton, M. L. Schneider, P. Kabos, T. J. Silva, and J. P. Nibarger, J. Appl. Phys. **99**, 093909 (2006).
[34] I. Neudecker, G. Woltersdorf, B. Heinrich, T. Okuno, G. Gubbiotti, and C. Back, J. Magn. Magn. Mater. **307**, 148 (2006).
[35] C. Bilzer, T. Devolder, P. Crozat, C. Chappert, S. Cardoso, and P. P. Freitas, J. Appl. Phys. **101**, 074505 (2007).
[36] J.-M. L. Beaujour, W. Chen, C.-C. Krycka, K. Kao, J. Sun, and A. Kent, Eur. Phys. J. B **59**, 475 (2007).
[37] G. Counil, J.-V. Kim, K. Shigeto, Y. Otani, T. Devolder, P. Crozat, H. Hurdequint, and C. Chappert, J. Magn. Magn. Mater. **272-276**, 290 (2004).
[38] M. Bailleul, R. Höllinger, and C. Fermon, Phys. Rev. B **73**, 104424 (2006).
[39] S. M. Seo, K. J. Lee, H. Yang, and T. Ono, Phys. Rev. Lett. **102**, 147202 (2009).
[40] M. Bailleul, Ph.D. thesis, Ecole Polytechnique, 2002; http://www-ipcms.u-strasbg.fr/IMG/pdf/these_bailleul_2002.pdf

[41] Note that the results of such calculations for the self-inductance of much wider antennae and for magnetostatic surface waves had been reported in Refs. 9 and 40.

[42] $L_{equ}(k,\omega)$ has the dimension of a linear inductance. $kL_{equ}(k,\omega)$ can be interpreted as the self-inductance per unit surface for a perfectly monochromatic antenna (infinitely extended harmonic distribution of current).

[43] Note that the magnetic film thickness t was given different values for the four devices, ranging from 17 to 19 nm. This parameter is critical in setting the spacing between the main and secondary absorption peaks, which does not depend strongly on the value of the other parameters. We attribute the different values to a slight and inhomogeneous degradation of the film during the fabrication process. These differences were also obtained when following precisely the position of the main and secondary self-inductance absorption peaks as a function of the external field (Ref. 7).